Deep Optical CCD Observation on Supernovae Remnants

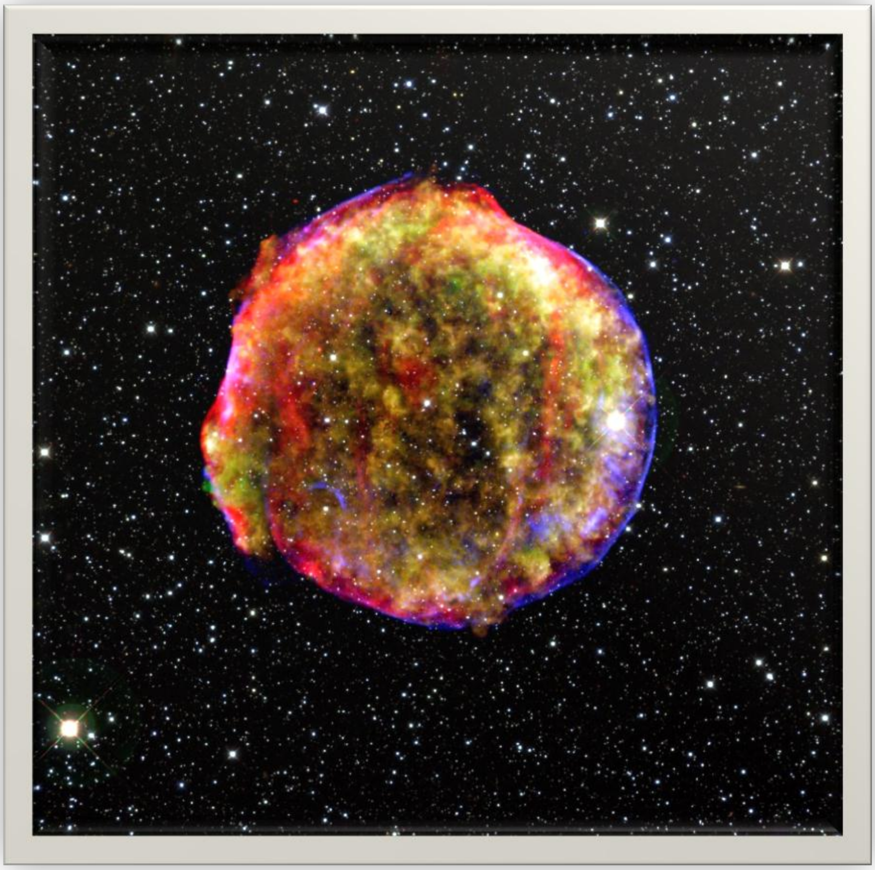

Konstantinos Kouroubatzakis

Aristotle University of Thessaloniki
Department of Physics
Section of Astrophysics, Astronomy and Mechanics

Diploma Thesis 2011

Deep Optical CCD Observation on Supernovae Remnants

Supervisor: **Professor John. H. Seiradakis**

Konstantinos Kouroubatzakis

Aristotle University of Thessaloniki
Department of Physics
Section of Astrophysics, Astronomy and Mechanics

Diploma Thesis 2011

To the giants whose shoulders we stand on

Abstract

This diploma thesis refers mostly to practical issues of observational astronomy and to learning how to conduct deep optical observations with CCD cameras.

It is divided in to three main chapters. The first chapter contains an introduction on Supernovae and Supernovae remnants and their main principles. In the second chapter the practical part of the diploma thesis is developed, showing how the observations were performed. And in the third and final chapter the photographic results of this diploma thesis and their analysis are presented.

Acknowledgements

As this diploma thesis signals the completion of my studies for the bachelor degree in physics, the first persons I need to thank are my family who supported me psychologically and financially throughout the way.

I feel privileged for the opportunity to be one of the students of Professor John. H. Seiradakis. He helped me in any possible manner during this diploma thesis and was a great teacher for a variety of things the past years.

I could not forget to mention Professor Stauros Augoloupis who in first place gave a great boost for my love in astronomy.

A lot of thanks to Professor Fotis Mauromatakis who helped us deciding what would be the best choice for supplying the Holomon Astronomical Station with the best possible filters.

Also, many thanks to the stuff of the Department of Forestry and Natural Environment (DFNE) at Mt. Holomon, Khalkidhiki, and especially to its Director, Mr Panourias George and its curator, Papanikolaou Christos.

And last but not least I want to thank the whole team of the laboratory of observational astronomy in A.U.Th. but mostly the companions, co-students John Vakoulis, Vassilis Karamanavis, Thanassis Nitsos and John Antoniadis who helped me during my involvement in every possible way.

Contents

List of figures

List of tables

Chapter 1: About Supernovae and Supernovae Remnants

1.1 Supernovae Classification

The stars that are observed as novae and those that explode as supernovae stars belong to the category of catastrophic variables, with main characteristic the rapid (in hours or days) growth of their illumination, sometimes over ten magnitudes. The initial classification of the objects is based on observational data in the manner that is shown in table 1.1

Type	M min	ΔM	Log (E) (ergs)	Period	Hydrogen Lines	Typical representative
SN I	-19	>20	51	-	No	Tycho
SN II	-17	?	50	-	Yes	Cas A, 1987A
Novae	-10 <M< -5	10	44	100 years	-	Nova Persei
Dwarf Novae	-	5	38	100 days	-	U Gemini-norum

Table 1.1Classification of catastrophic variables

The theories that are proposed to explain novae and supernovae can be divided in two basic categories:

A) In those that refer to the evolution of single stars with large mass **(Type II supernovae)** and
B) in those that refer to the evolution of double star systems of medium mass (**Type I supernovae and novae)**

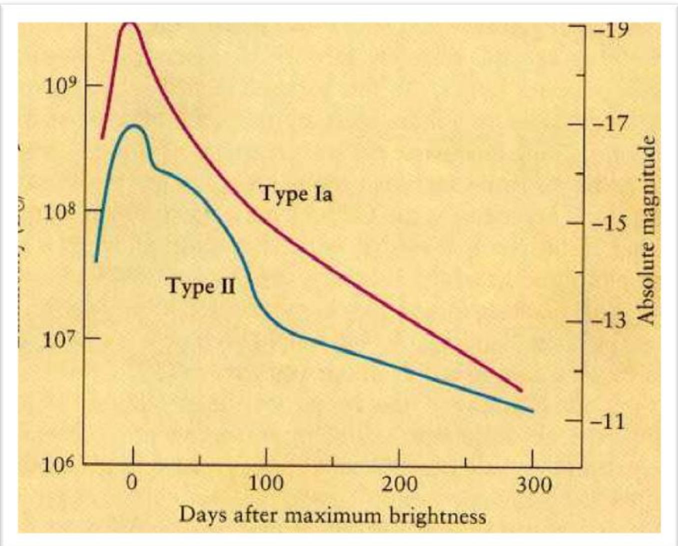

Figure 1.1 Characteristic light curves of Type I and Type II Supernovae.

Type II supernovae

The catastrophic collapse of the star's iron core, the generation of a shock wave, and the ensuing ejection of the star's envelope, are believed to be the basic mechanism that creates a Type II supernovae. Observationally Type II Supernovae are characterized by a rapid rise in luminosity reaching a limiting absolute bolometric magnitude of about -18, followed by a steady decrease, dropping six to eight magnitudes in a year. Their spectra also exhibit lines associated with hydrogen and heavier elements.

Single stars with mass $M > 5M_{\odot}$ will end their life with Type II supernovae. For stars with total mass is $5M_{\odot} < M < 10M_{\odot}$, the mass of the inactive carbon core is big enough to reach the high temperature that is needed to start the carbon fission process.

$$^{12}C + {}^{12}C \longrightarrow {}^{24}Mg$$

$$^{12}C + {}^{12}C \longrightarrow {}^{20}Ne \ + \ a$$

$$^{12}C + \ a \longrightarrow {}^{16}O$$

The result is a Type II supernova and the creation of neutron star or even the complete demolition of the core.

Stars whose mass exceeds ten solar masses, $M > 10M_{\odot}$, will also end their life with a Type II supernovae explosion. Such stars that have exhausted all available nuclear resources and have created an iron core start to collapse since there is no internal force to compensate the gravitational pressure. The core's mass exceeds the Chandrasekhar limit so the collapse will not stop with the creation of a White Dwarf. It will continue until the core reaches states of higher density. The adiabatic compression of the core results in a sharp rise of the temperature, which also results in the iron **photodisintegration** according to the following reactions.

$$^{56}Fe + h\nu \longrightarrow 13\ {}^{4}He + 4n$$

$$^{4}He + h\nu \longrightarrow 2p + 2n$$

These reactions absorb energy, stop the core's temperature and pressure rise and speed up the collapse. At this point there are two possible solutions

a) The initial star mass is over 25 solar masses $M > 25M_{\odot}$. At this case gravity is always bigger than the internal pressure and nothing stops the collapse. The star catastrophically collapses to a **Black Hole**.
b) The initial star mass is near 10 solar masses $M \simeq 10M_{\odot}$. At this case the pressure growth cannot continue forever and there is a point that the

internal pressure exceeds the gravitational pressure and the external layers "bump" starting to expand with supersonic speed. During the expansion a shock wave is created that heats up and sends outwards the outer layers that continue to collapse. Simultaneously there is a great abundance in neutrons, which are absorbed by medium –atomic number elements and create heavier elements that cannot be created in exothermic nuclear reactions. It is believed that the central piece of the initial core usually stabilize in a neutron star condition.

It must be mentioned that the natural mechanism of supernovae explosions and the mass limit beyond of which a star leads to the creation of a black hole is not completely known.

Novae and Type I supernovae

According to the most accepted scenario, novae come from the evolutions of double star systems. In a double star system with stars 1 and 2 that have masses $M_1 > M_2$, star 1 is the first to leave the main sequence and starts to evolve into a **Red Giant**. If the distance of the two stars is small enough, mass from the outer layers of star 1 is transported to the Roche lob and from there to star 2. When this process is over the only part of star 1 that is left is the initial core that usually turns to a white dwarf with $M \simeq 1M_{\odot}$. Star 2 has become a lot larger and starts to evolve in to a red giant. During this evolution star 2 fills its own Roche lob and the reverse process of transporting mass from star 2 to star 1 is initiated.

When the mass of the matter that accumulates in the hot white dwarfs atmosphere exceeds a critical point, the pressure and the temperature at the base of the atmosphere allows the transmutation of Hydrogen to Helium. This reaction occurs instantly and the energy is released in the form of a big explosion. According to this scenario all novae are double and consecutively repeated.

For the type I supernovae the most acceptable theory is similar to that of novae with the difference that there is a double star system with one of its members being a carbon-oxygen white dwarf. The process continues similar to the novae scenario but here the white dwarfs mass exceeds the Chandrasekhar limit and the transmutation occurs extremely rapidly($\sim 1s$). The produced energy heats up and ejects the upper layers of the star towards the empty space. This kind of explosion demolishes the system and is so powerful that leaves no compact stellar object.

1.2 Supernovae Remnants (SNRs)

The remains of a supernovae explosion are a supernovae remnant (SNR). The SNRs are extremely important for understanding the universe as they perform important functions. They heat up the interstellar medium, distribute heavy elements throughout the Galaxy, and accelerate cosmic rays. We can separate the life of a SNR in three main stages.

In the first phase, free expansion, the front of the expansion is formed from the shock wave interacting with the ambient **Interstellar Medium (ISM).** This phase is characterized by constant temperature within the SNR and constant expansion velocity of the shell. It lasts a couple hundred years.

During the second phase, known as the *Sedov* or *Adiabatic* Phase, the SNR material slowly begins to decelerate by $\sim r^{-3/2}$ and cool by $\sim r^{-3}$ (r being the radius of the SNR). In this phase, the main shell of the SNR is **Rayleigh-Taylor** unstable, and the SNR's ejecta becomes mixed up with the gas that was just shocked by the initial shock wave. This mixing also enhances the magnetic field inside the SNR shell. This phase lasts 10,000 - 20,000 years.

The third phase, the *Snow-plow* or *Radiative* phase, begins after the shell has cooled down to about 10^6 K. At this stage, electrons begin recombining with the heavier atoms (like oxygen) so the shell can more efficiently radiate energy. This, in turn, cools the shell faster, making it shrink and become denser. The more the shell cools, the more atoms can recombine, creating a snowball effect. Because of this snowball effect, the SNR quickly develops a thin shell and radiates most of its energy away as optical light. The velocity now decreases as $\sim r^{-3}$. Outward expansion stops and the SNR start to collapse under its own gravity. This lasts a few hundreds of thousands of years. After millions of years, the SNR will be absorbed into the interstellar medium due to Rayleigh-Taylor instabilities breaking material away from the SNR's outer shell.

The SNRs are classified in three main categories, the shell type, crab style and composite remnants.

A) Shell type remnants

As the shock wave from the supernova explosion plows through space, it heats and stirs up any interstellar material it encounters, thus producing a big shell of hot material in space. We see a ring-like structure in this type of SNR because when we look at the edge of the shell, there is more hot gas in our line of sight than when we look through the middle. This phenomenon is called limb brightening.

B) Crab style remnants

These remnants (also called pulsar wind nebulae, or plerions) look more like a "blob" than a "ring", in contrast to the shell-like remnants. The plerions are filled with high-energy electrons that are flung out from a **pulsar** in the middle. These electrons interact with the magnetic field by synchrotron radiation and emit X-rays, visible light, and radio waves. The most famous plerion is the *Crab Nebula*, hence the common name, Crab-like remnants.

C) Composite remnants

These remnants are a cross between the shell-type remnants and crab-like remnants. They appear shell-like, crab-like or both depending on what part of the electromagnetic spectrum one is observing them in. There are two kinds of composite remnants -- thermal and plerionic

Thermal composites

These SNRs appear shell-type in the radio waveband (synchrotron radiation). In X-rays, however, they appear crab-like, but unlike the true crab-like remnants their X-ray spectra have spectral lines, indicative of hot gas.

Plerionic composites

These SNRs appear crab-like in both radio and X-ray wavebands; however, they also have shells. Their X-ray spectra in the center do not show spectral lines, but the X-ray spectra near the shell do have spectral lines.

Figure 1.2 The well known shell type bright SNR Cas A.

Figure 1.3 The well known bright SNR Crab Nebulae.

1.3 Forbidden lines

We call forbidden lines the spectral lines emitted by atoms undergoing energy transitions that not normally allowed by the selection rules of quantum mechanics. Although the transitions are nominally "forbidden", there is a small probability of their spontaneous occurrence. Such an excited atom will make a forbidden transition to a lower energy state per unit time. Nevertheless, "forbidden" transitions are only relatively unlikely, states that can only decay in this way (so-called meta-stable states) usually have lifetimes of the order milliseconds to seconds, compared to less than a microsecond for decay via permitted transitions.

Forbidden emission lines have only been observed in extremely low-density gases and plasmas, either in outer space or in the extreme upper atmosphere of the Earth. Even the hardest laboratory vacuum on Earth is still too dense for forbidden line emission to occur before atoms are collisionally de-excited. However, in space environments, densities may be only a few atoms per cubic centimeter, making atomic collisions unlikely. Under such conditions, once an atom or molecule has been excited for any reason into a meta-stable state, then it is almost certain to decay by emitting a forbidden-line photon. Since meta-stable states are rather common, forbidden transitions account for a significant percentage of the photons emitted by the ultra-low density gas in space.

Forbidden line transitions are noted by placing square brackets around the atomic or molecular species in question, e.g. $[O_{II}]$, $[O_{III}], [S_{II}]$,. Forbidden lines of nitrogen ($[N_{II}]$at 654.8 and 658.4 nm), sulfur ($[S_{II}]$at 671.6 and 673.1 nm), and oxygen ($[O_{II}]$ at 372.7 nm, and $[O_{III}]$at 495.9 and 500.7 nm) are commonly observed in astrophysical plasmas. These lines are extremely important to the energy balance of such things as planetary nebulae and H II regions. Also, the forbidden 21-cm hydrogen line is of the utmost importance for radio astronomy as it allows very cold neutral hydrogen gas to be seen.

1.4 Emission lines of Supernovae Remnants

At present there are approximately 270 Galactic SNR's that have been observed, mostly in radio wavelengths, and are described in David Green's Catalog. The great majority of these are believed to be relatively old in either the adiabatic or the early radiative stages of their evolutionary development. Such remnants have ages greater than 10^3 and radius larger than $\sim$5 pc, and generally show a characteristic shell structure of nonthermal radio emission.

About sixty SNRs have known optical emission associated with their nonthermal radio emission (Van den Bergh 1983). For old remnants this optical emission arises from the cooling of shocked interstellar cloud material following passage of the remnant's blast wave as it expands outwards into the ambient medium. Spectra of filaments of evolved SNRs over the wavelength range 3500-7000 $\dot{A}$ show strong lines of H, $[O_{II}]$, $[O_{III}], [S_{II}]$, and $[N_{II}]$ with generally fainter lines of He_I, He_{II} $[O_I], [N_I], [N_{III}], [Fe_{II}], [Fe_{III}], [Ca_{II}] and\ [Ar_{III}]$. In contrast to the situation for young remnants such as Cas A and the Crab Nebula, where there is element enrichment from the supernovae ejecta, older SNR abundances seem to reflect that of the ambient interstellar medium, although with varying degrees of grain destruction (Raymond 1983).

A multiwavelength approach is necessary to identify a source as a SNR, since an observation through a single spectral window cannot identify all types of SNRs. The three wavelength regimes that have been used most commonly for SNR surveys have been the X-ray, optical, and radio domains (see Magnier et al. 1995 for a review). A SNR can be a prominent source in each of these bands for different reasons. The expanding SNR shock heats the surrounding ISM to temperatures of $10^6 - 10^7 K$, producing X-ray emission (e.g., Itoh & Masai 1989), while electrons gyrating in the SNR's magnetic field produce synchrotron radiation at radio frequencies (e.g., Duric et al. 1995). A SNR can also be detected optically by emission from collisionally ionized species such as $[N_{II}]$, $[O_{III}], [S_{II}]$, as well as Ha recombination emission. The degree to which a SNR becomes an X-ray, radio or optical emission line source and the relative strengths of each of these radiative signatures are most likely a function of environment and the evolutionary stage of the SNR. The details, however, are poorly understood.

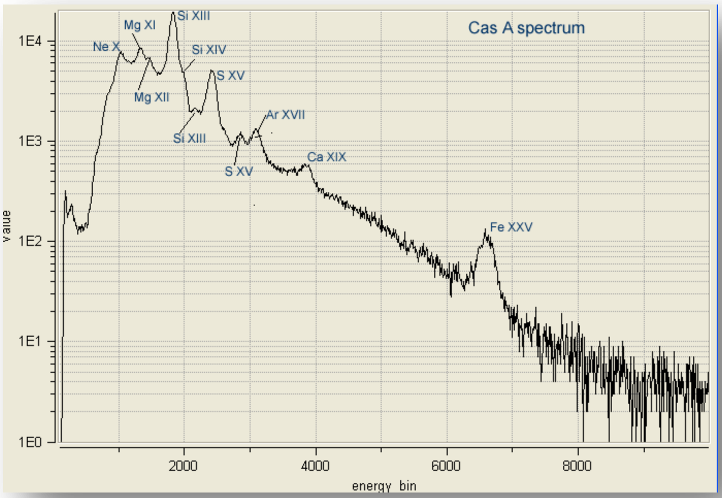

Figure 1.4 SNRs Cas A Spectrum.

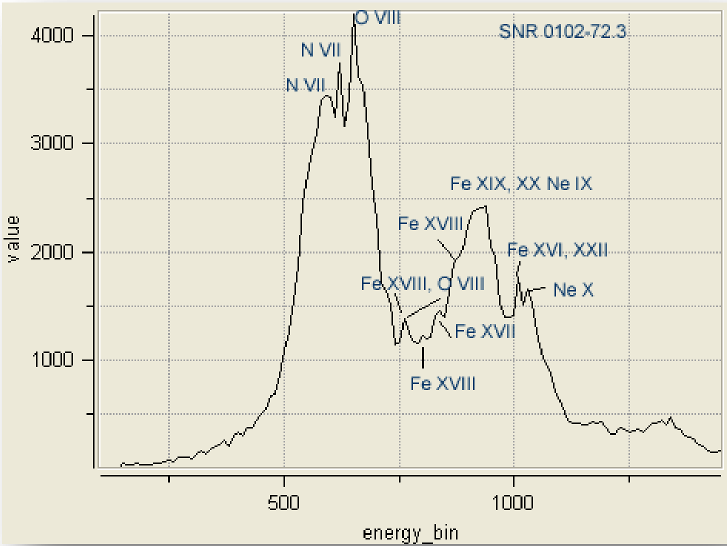

Figure 1.5 SNR 0102-72.3 (Located in Small Maggelanic Cloud) Spectrum.

1.5 Optical detected galactic SNRs

Until this moment approximately sixty galactic SNRs that have been studied present optical emission. Those are listed in the table below.

SNR Galactic Coordinates (other names)	RA	Dec
G4.5+6.8	$17^h30^m42^s$	$-21^\circ 29'$
G5.4-1.2 (Milne 56)	$18^h02^m10^s$	$-24^\circ 54'$
G6.4-0.1	$18^h00^m30^s$	$-23^\circ 26'$
G13.3-1.3	$18^h19^m20^s$	$-18^\circ 00'$
G15.1-1.6	$18^h24^m00^s$	$-16^\circ 34'$
G17.4-2.3	$18^h30^m55^s$	$-14^\circ 52'$
G31.5-0.6	$18^h51^m10^s$	$-01^\circ 31'$
G34.7-0.4 (W44, 3c392)	$18^h56^m00^s$	$+01^\circ 22'$
G39.7-2.0 (W50, SS433)	$19^h12^m20^s$	$-04^\circ 55'$
G49.2-0.7 (W51)	$19^h23^m50^s$	$-14^\circ 06'$
G53.6-2.2 (3C400.2, NRAO 611)	$19^h38^m50^s$	$+17^\circ 14'$
G54.4-0.3 (HC40)	$19^h33^m20^s$	$+18^\circ 56'$
G59.5+0.1	$19^h42^m33^s$	$+23^\circ 35'$
G59.8+1.2	$19^h38^m55^s$	$+24^\circ 19'$
G65.3+5.7	$19^h33^m00^s$	$+31^\circ 10'$
G67.7+1.8	$19^h54^m32^s$	$+31^\circ 29'$
G69.0+2.7	$19^h53^m20^s$	$+32^\circ 55'$
G73.9+0.9	$20^h14^m15^s$	$+36^\circ 12'$
G74.0-8.5 (Cygnus Loop)	$20^h13^m00^s$	$+30^\circ 40'$
G78.2+2.1 (DR4, γ Cygni SNR)	$20^h20^m50^s$	$+40^\circ 26'$
G82.2+5.3 (W63)	$20^h19^m00^s$	$+45^\circ 30'$
G89.0+4.7 (HB61)	$20^h45^m00^s$	$+50^\circ 35'$
G111.7-2.1 (Cassiopeia A)	$23^h23^m26^s$	$+50^\circ 35'$
G114.3+0.3	$23^h37^m00^s$	$+61^\circ 22'$
G116.5+1.1	$23^h53^m40^s$	$+63^\circ 15'$
G116.9+0.2 (CTB 1)	$23^h59^m10^s$	$+62^\circ 26'$
G119.5+10.2 (CTA 1)	$00^h06^m40^s$	$+72^\circ 45'$
G120.1+1.4 (Tycho, 3C10, SN1572	$00^h25^m18^s$	$+64^\circ 09'$
G129.2+1.6	$01^h22^m00^s$	$+64^\circ 15'$
G127.1+0.5 (R5)	$01^h28^m20^s$	$+63^\circ 10'$
G130.7+3.1 (3C58, SN1181)	$02^h05^m41^s$	$+64^\circ 49'$
G132.7+1.3 (HB3)	$02^h17^m40^s$	$+62^\circ 45'$
G156.2+5.7	$04^h58^m40^s$	$+51^\circ 50'$
G160.9+2.6 (HB9)	$05^h01^m00^s$	$+46^\circ 40'$
G166.0+4.3 (VRO 42.05.01)	$05^h26^m30^s$	$+42^\circ 56'$
G180.0-1.7 (S147)	$05^h39^m00^s$	$+27^\circ 50'$
G184.6-5.8 (Crab Nebulae, 3C144, SN1054)	$05^h34^m31^s$	$+22^\circ 01'$
G189.1+3.0 (IC443, 3C157)	$06^h17^m00^s$	$+22^\circ 34'$
G192.8-1.1 (PKS 0607+17	$06^h09^m20^s$	$+17^\circ 20'$

G205.5+0.5 (Monoceros Nebulae)	$06^h39^m00^s$	$+06^\circ30'$
G206.9+2.3 (PKS 0646+06)	$06^h48^m40^s$	$+06^\circ26'$
G260.4-3.4 (Puppis A, MSH 08-44)	$08^h22^m10^s$	$-43^\circ00'$
G263.9-3 (Vela)	$08^h34^m00^s$	$-45^\circ50'$
G266.2-1.2 (RX J0852.0-4622)	$08^h52^m00^s$	$-46^\circ20'$
G272.2-3	$08^h52^m00^s$	$-46^\circ20'$
G290.1-0.8	$11^h03^m05^s$	$-60^\circ56'$
G292.0+1.8 (MSH11-54)	$11^h24^m36^s$	$-59^\circ16'$
G296.1-0.5	$11^h51^m10^s$	$-62^\circ34'$
G296.1-0.5	$11^h51^m10^s$	$-62^\circ34'$
G296.5+10.0 (PKS 12.9-51/52)	$12^h09^m40^s$	$-52^\circ25'$
G299.2-2.9	$12^h15^m13^s$	$-65^\circ30'$
G315.1+2.7	$14^h24^m30^s$	$-57^\circ50'$
G315.4-2.3 (RCW 86, MSH 14-63)	$14^h43^m00^s$	$-62^\circ30'$
G320.4-1.2 (RCW 89, MSH15-52)	$15^h14^m30^s$	$-59^\circ08'$
G326.3-1.8 (MSH 15-56)	$15^h53^m00^s$	$-56^\circ10'$
G327.6+14.6 (SN1006, PKS1459-41)	$15^h02^m50^s$	$-41^\circ56'$
G332.4-0.4 (RCW 103)	$16^h17^m33^s$	$-51^\circ02'$
G332.5-5.6	$16^h43^m20^s$	$-54^\circ30'$
G338.1+0.4	$16^h37^m59^s$	$-46^\circ24'$
G340.6+0.3	$16^h47^m41^s$	$-44^\circ34'$
G343.1-2.3 (RCW 114)	$17^h25^m00^s$	$-46^\circ30'$

Table 1.2 Optical detected galactic SNRs

1.6 Introduction to SNRs Detection Process

The optical detection of SNR is a process that has a lot of demands. All the galactic SNRs that have been detected are on or close to the galactic disk where most of the galaxys dust is placed. Optical light emmited by these usually faint objects is being absorbed or scattered by the galactic dust as it travels through the large galactic distances, much more than at radio wavelgths. This can also explain why only about one fifth of the SNRs that have been observed at radio waves have been detected in optical wavelengths.

The overcrowded regions of the galactic disk where most of the SNRs are found, creates one more difficulty. Various other objects, like stellar nebulas, sometimes can be projected in the same region of the sky and must be subtracted in order to reveal the SNR.

Also another challenge comes from the small amount of SNR's light that reaches us. This demands long exposures in order to collect a sufficient amount of this light.

Figure 1.6 In this figure we see the sky region of SNR G82.2+ 5.3 observed in white light. The bright nebula shown is not related with the SNR and has to be subtracted.

1.7 Detection of SNRs OIII emission lines

Doubly ionized oxygen (also known as $[O_{III}]$) emits strong forbidden in the green part of the spectrum primary at the wavelength of 500.7 nm and secondarily at 495.9 nm. Consequently, narrow band-pass filters that isolate the 500.7 nm and 496 nm wavelengths of light are useful in observing these objects, causing them to appear at higher contrast against the filtered and consequently blacker sky background where the $[O_{III}]$ frequencies are much less pronounced.

Chapter 2: Observations, Instrumentation and Data Reduction

2.1 Instrumentation

2.1.1 The Telescopes

The observations were carried out with a *Takahashi Epsilon 180ED* astrograph, mounted on Orion *Atlas EQ-G* or a *Celestron CGE Pro* mounts. The *Epsilon-180ED* is a catadioptric reflector, including a hyperbolical primary mirror, an elliptical secondary mirror and a 2-lenses field corrector in the rack-and-pinion focuser. The co a configuration produces a perfectly flat field, ideal for wide field imaging.

***Takahashi Epsilon 180ED* specifications**	
Optical design	Hyperbolical Newton
Effective aperture	180mm
Primary mirror diameter	190mm
Secondary mirror (minor axis)	80mm
Focal length	500mm
Focal ratio	f/2.8
Resolution	0.64"
Limiting magnitude (visual)	13.0
Image circle	44mm (60% not vignetted)
Back focus (BFL)	56mm (from the end of the corrector)

Table 2.1 Takahashi Epsilon 180ED specifications

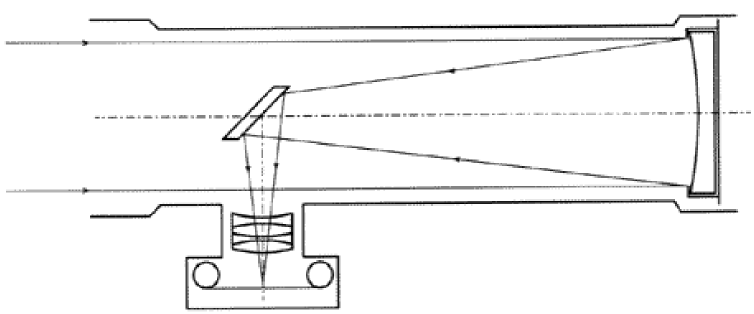

Figure 2.1 Epsilon 180 ED design

Figure 2.2 Spots diagram: The diffraction pattern almost does not present a residue of coma in periphery. In the same way, the 2-lenses corrector practically does not generate any chromatism.

We also used a 114 mm diameter f/4.3 Konus F.L. 500 Reflector for guiding purposes.

2.1.2 The Cameras

A Fingerlakes Pro Line 6303E camera was used to record the observations and an Imaging Source DMK 21 monochrome camera to carry out the main telescope guiding process.

Figure 2.3 Imaging Source DMK 21 camera

Fingerlakes Pro Line 6303E specifications	
Sensor	KAF-6303E (Kodak)
Array size	3072 x 2048
Pixel size	9 µm
Typical maximum cooling	70º C Below ambient
Typical download speeds @ 16-bit	1 MHz, 8 MHz (other speeds available)
Typical system noise	9 e- RMS @ 1 MHz
Nonlinearity	<1%
Operating environment	-30º C - 45º C | 10% - 90% Relative Humidity
Sensor manufacturer	Kodak
CCD grades available	2
CCD type	Front illuminated
Color/Monochrome	Monochrome
Mega pixels	6.3
Sensor diagonal	33.3 mm
Linear full well	100,000 e-
Typical dark current	<0.005 e-/pixel/sec. @ -45º C
Anti blooming	None
Available shutters (optional)	65 mm
Shutter MTBF	1,000,000
Remote triggering	Standard
Power	12v
Interface	USB 2.0
Gain @ 2 * 2 Binning (Calculated)	2.108
Readout Noise (Calculated)	12.920

Table 2.2 Fingerlakes Pro Line 6303E specifications

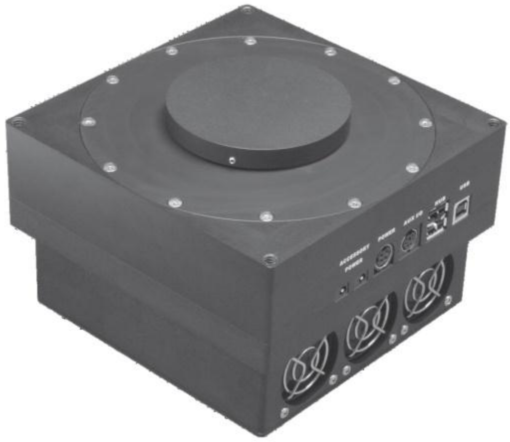

Figure 2.4 FLI Pro line 63603E Camera

2.1.3 Field of View Calculation

We can calculate the field of view of the current telescope-camera configuration using the following equations.

$$FOV(Arcmin) = \frac{3438\,S}{f}$$

$$S \equiv Chip\ Dimension$$
$$f \equiv telescopes\ focal\ length = 504mm$$
$$S_a = 3072 \cdot 9 \cdot 10^{-3}mm = 30.942mm$$
$$S_b = 2048 \cdot 9 \cdot 10^{-3}mm = 18.432mm$$

$$FOV(Arcmin) = 0.06139 * 0.03657 \Rightarrow FOV(degrees) = 3.6835^{\circ} * 2.1942^{\circ}$$

2.1.4 The filters

In order to record the doubly ionized line of oxygen we used two special filters. The main filter was a symbolometric narrow band filter, centered at 500.7 nm, with a FWHM of 4 nm and the second was the *y* filter of the *Stromgren* line used for background light subtraction.

Filter	$[O_{III}]$	*stromgren y*
Edges - Cut on	498.7 nm	535 nm
Edges - Cut of	502.7 nm	560 nm
Peak Transmission	70%	80%
FWHM	3nm	23nm

Table 2.3 Filter's specifications

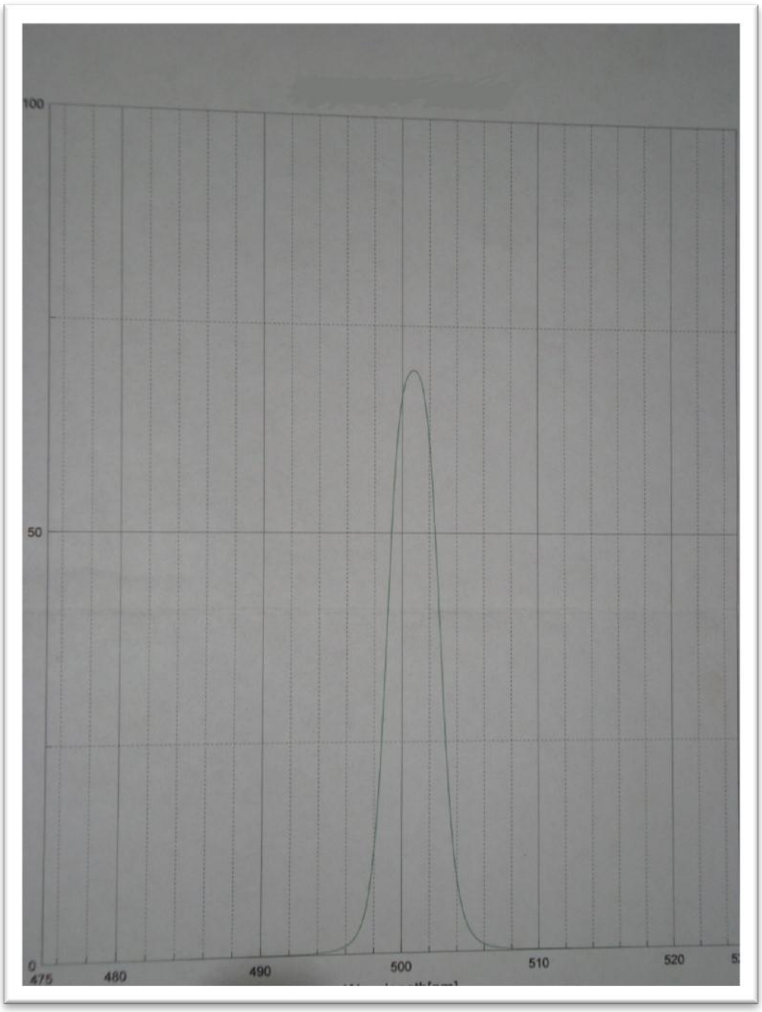

Figure2.5 $[O_{III}]$ filter's transmission diagram given by the manufacturer.

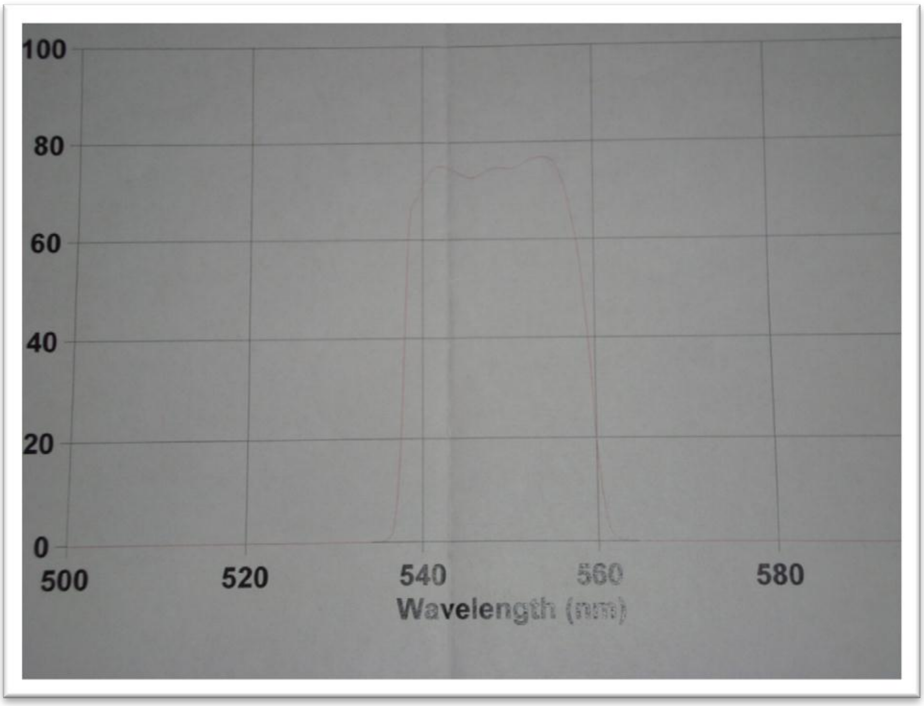

Figure2.6 The Stromgren y filter’s transmission diagram given by the manufacturer.

2.2 Observations

2.2.1 Observations location

The observations were carried out at the Holomon astronomical station, located on the Mount Holomon in Khalkidhiki peninsula, in the Aristotle's University forest of Taxiarhis. The site has very good astronomical properties, being away of the light polluted areas it has a measured median value of seeing $\sim 0.82''$

Holomon Astronomical Station	
Longitude	$-23^{\circ}30'19.6''$(East)
Latitude	$+40^{\circ}25'58.4''$ (North)
Elevation	$\sim 800\ m$
Hottest months	July, August (temperature can reach up to $36^{\circ}C$
Coldest months	January, February (temperature can reach down to $-15^{\circ}C$
Annual rainfall height	$\sim 750mm$
Median value of seeing	$\sim 0.82''$

Table 2.4

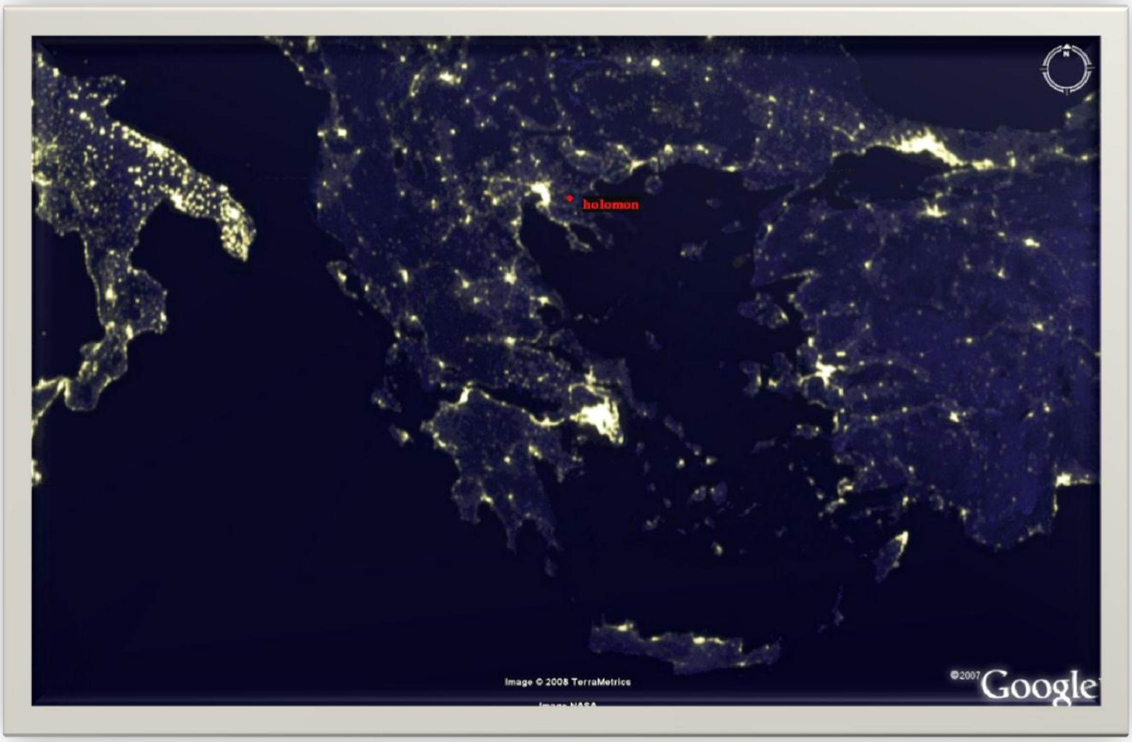

Figure 2.7 The light pollution map of Greece.

2.2.2 Data Recording Software

In order to record the observational data, we used the Maxim DL 5 and IC Capture AS astronomical software. Maxim DL 5 were receiving the data with the main camera Fingerlakes Pro line 63603E and guiding was achieved with IC Capture AS and DMK 21.

2.2.3 The Targets

G74.0-8.5 –Cygnus Loop

1-GHz flux/Jy: 210
Size/arcmin: 230×160
Spectral index: varies
Type: S
Has been suggested that this is two overlapping remnants.
Radio: Shell, brightest to the NE, with fainter breakout region to S, with spectral variations.
Optical: Large filamentary loop, brightest to the NE, not well defined to the S or W.
X-ray: Shell in soft X-rays.
Point sources: Several compact radio sources within the boundary of the remnant, including CL4, plus X-ray
sources in S.
Distance: Optical proper motion and shock velocity gives 0.44 kpc.

References:

Green 1990, AJ, 100, 1927. DRAO at 408 MHz (30 .3×60 .7) for spectral index study, plus X-ray and optical.
Graham et al. 1991, AJ, 101, 175. Shocked molecular H outside rim in NE.
Shull & Clarke 1991, PASP, 103, 811. Optical spectroscopy of nearside filaments.
Greidanus & Strom 1992, A&A, 257, 265. Optical kinematics.
Shull & Hippelein 1992, ApJ, 383, 714. Optical kinematics and proper motion.
Fesen et al. 1992, AJ, 104, 719. Ha imagery.
Cornett et al. 1992, ApJ, 395, L9. UV imagery.
Long et al. 1992, ApJ, 400, 214. Optical of Balmer dominated filament.
Arendt et al. 1992, ApJ, 400, 562. IRAS observations.
Hester et al. 1994, ApJ, 420, 721. Ha, [OIII] and other optical observations of Balmer dominated filaments in NE.
Gorham et al. 1996, ApJ, 458, 257. Pulsar search.
Biggs & Lyne 1996, MNRAS, 282, 691. Pulsar search.
Levenson et al. 1997, ApJ, 484, 304. ROSAT observations.
Leahy et al. 1997, AJ, 114, 2081. DRAO at 1.4 GHz (10×20), including polarisation.
Miyata et al. 1998, PASJ, 50, 257. ASCA observations.
Miyata et al. 1998, PASJ, 50, 475. ASCA observations of compact X-ray source in S.

Leahy & Roger 1998, ApJ, 505, 784. DRAO at 1.4 GHz (10 .0×10 .9) and 408 MHz (30 .4×60 .9), for spectral index studies in comparison with
other radio observations.
Levenson et al. 1998, ApJS, 118, 541. Optical images.
Roger et al. 1999, A&AS, 137, 7. 22 MHz flux density (S =1400±400 Jy).
Bohigas et al. 1999, ApJ, 518, 324. Optical spectroscopy of surroundings.
Levenson et al. 1999, ApJ, 526, 874. ROSAT images.
Blair et al. 1999, AJ, 118, 942. HST observations, for distance.
Aschenbach & Leahy 1999, A&A, 341, 602. ROSAT image, and comparison with radio.
Sauvageot et al. 1999, A&A, 351, 669. [NeV] observations.
Szentgyorgyi et al. 2000, ApJ, 529, 279. [NeV] images.
Danforth et al. 2000, AJ, 119, 2319. UV, optical and X-ray comparison of selected regions.
Sankrit et al. 2000, AJ, 120, 1925. HST far-UV spectra on non-radiative shock.
Miyata et al. 2001, ApJ, 550, 1023. ASCA observations of compact X-ray sources.
Miyata & Tsunemi 2001, ApJ, 552, 624. ASCA spectroscopy of regions in N and E.
Ghavamian et al. 2001, ApJ, 547, 995. Optical spectroscopy.
Danforth et al. 2001, AJ, 122, 938. Far-UV spectroscopy, Ha and other optical observations of NE region.
Levenson & Graham 2001, ApJ, 559, 948. HST of SE region.
Uyanıker et al. 2002, A&A, 389, L61. Effelsberg 100-m at 2.7 GHz (40 .3) including polarisation, and comparison with ROSAT data.
Leahy 2002, AJ, 123, 2689. DRAO at 1.4 GHz (40×20) for HI.
Patnaude et al. 2002, AJ, 124, 2118. Optical and ROSAT observations of region in SW.
Blair et al. 2002, ApJS, 140, 367. UV spectroscopy.
Welsh et al. 2002, A&A, 391, 705. Optical absorption to background stars.
Sankrit & Blair 2002, ApJ, 565, 297. UV observations of NE filament.
Levenson et al. 2002, ApJ, 576, 798. Chandra observations of W edge.
Reich et al. 2003, A&A, 408, 961. Effelsberg 100-m at 863 MHz (140 .5 : S =184±18 Jy).
Leahy 2004, MNRAS, 351, 385. Chandra observations of SW.
Uyanıker et al. 2004, A&A, 426, 909. Effelsberg 100-m at 2.7 GHz (40 .3), with comparison with other data for spectral index studies.
Blair et al. 2005, AJ, 129, 2268. HST of outer filaments.
Leahy 2005, AJ, 130, 165. DRAO at 1.4 GHz of SE.
Levenson & Graham 2005, ApJ, 622, 366. Chandra observations of know in SE.
Sun et al. 2006, A&A, 447, 937. Urumqi 25-m at 4.8 GHz (90 .5 : S =90±9 Jy), with comparisons with other data for spectral index studies.
Kaplan et al. 2006, ApJS, 163, 344. X-ray upper limit on compact sources.
Seon et al. 2006, ApJ, 644, L175. Far UV observations.
Sankrit et al. 2007, AJ, 133, 1383. UV observations of part.
Tsunemi et al. 2007, ApJ, 671, 1717. XMM observations of NE to SW.
Miyata et al. 2007, PASJ, 59, S163. Suzaku observations of NE.
Nemes et al. 2008, ApJ, 675, 1293. XMM observations of NE.
Katsuda et al. 2008, ApJ, 680, 1198. Chandra observations of NE.
Uchida et al. 2008, ApJ, 688, 1102. XMM observations.

G82.2+5.3

1-GHz flux/Jy: 120?
Size/arcmin: 95×65
Spectral index: 0.5?
Type: S
Has been called G82.5+5.3.
Radio: Shell in the Cygnus X complex.
Optical: In complex region, but spectra indicate SNR filaments.
X-ray: Detected.

References:
Velusamy & Kundu 1974, A&A, 32, 375. NRAO 300-ft at 2.7 GHz (50 : S =59.0±3.5 Jy).
Sabbadin 1976, A&A, 51, 159. Optical spectra.
Angerhofer et al. 1977, A&A, 55, 11. NRAO 140-ft at 5 GHz (60 .8). Incomplete mapping.
Rosado & Gonz´alez 1981, RMxAA, 5, 93. Optical spectra.
Seward 1990, ApJS, 73, 781. Einstein observations.
Biggs & Lyne 1996, MNRAS, 282, 691. Pulsar search.
Lorimer et al. 1998, A&A, 331, 1002. Pulsar search.
Reich et al. 2003, A&A, 408, 961. Effelsberg 100-m at 863 MHz (140 .5 : S =82.5±5.5 Jy).
Uyanıker et al. 2003, ApJ, 585, 785. CGPS at 1.4 GHz (10) including polarisation, of part.
Mavromatakis et al. 2004, A&A, 415, 1051. ROSAT, ASCA and optical observations.
Kothes et al. 2006, A&A, 457, 1081. CGPS at 408 MHz (_30 : S =144±12 Jy) and 1420 MHz (_10 : S =93±5 Jy), including review of flux densities.

G93.7-0.2

1-GHz flux/Jy: 65
Size/arcmin: 80
Spectral index: 0.65
Type: S
Has been called G93.6–0.2 and G93.7–0.3.
Radio: Distorted, faint shell.
Distance: Association with HI features suggests 1.5 kpc.

References:
Velusamy & Kundu 1974, A&A, 32, 375. NRAO 300-ft at 2.7 GHz (50 : S =18.4±1.0 Jy).
Mantovani et al. 1982, A&A, 105, 176. Effelsberg 100-m at 1.7 GHz (70 .6 : S =53.5±5.0 Jy), plus review of flux densities.
Landecker et al. 1985, AJ, 90, 1082. DRAO at 1.4 GHz (smoothed to 20 : S =58±6 Jy).
Mantovani et al. 1991, A&A, 247, 545. Effelsberg 100-m at 4.75 GHz (smoothed to 30 : S =33.5±4.0 Jy), including polarisation, plus review of flux densities.
Biggs & Lyne 1996, MNRAS, 282, 691. Pulsar search.
Lorimer et al. 1998, A&A, 331, 1002. Pulsar search.
Koralesky et al. 1998, AJ, 116, 1323. VLA search for OH emission.
Uyanıker et al. 2002, ApJ, 565, 1022. CGPS 1.4 GHz (5400×4900), including HI, and 408 MHz (30 .7×20 .8).
Uyanıker et al. 2003, ApJ, 585, 785. CGPS at 1.4 GHz (10) including polarisation.
Kothes et al. 2006, A&A, 457, 1081. CGPS at 408 MHz (_30 : S = 67±6 Jy) and 1420 MHz (_10 : S = 35±4 Jy), including polarisation and review of flux densities.

2.2.4 Observations Log

Target	**Exposure Time (sec)**	**Number of Frames**	**Filter**	**Binning**	**Chip Temperature ($^\circ C$)**	**Target Altitude ($^\circ$)**	**Date**
G82.2+5.3	1200	6	$[O_{III}]$	1	-35	39.65	07/13/2010
G82.2+5.3	1200	1	*stromgren y*	1	-35	43.36	07/14/2010
G93.7-0.2	1200	3	$[O_{III}]$	1	-35	86.41	07/12/2010
G93.7-0.2	1200	1	*stromgren y*	1	-35	39.17	07/14/2010
G74.0-8.5	600	3	$[O_{III}]$	1	-35	41.38	07/13/2010
G74.0-8.5	600	1	*stromgren y*	1	-35	58.51	07/14/2010

Table 2.5 Observations Log

2.3 Data Reduction

2.3.1 Introduction

The aim in CCD data reduction is to eliminate a) the noise and b) the unnecessary contributions that comes either from the recording system or contributions that come with the photons that interacted with our CCD chip during the exposure time (also in many cases cosmic radiation may have to be subtracted).

In this diploma thesis we had to perform the basic CCD Data reduction, needed in all cases of CCD observations and also the continuum subtraction process needed when we use narrow band filters for our observations. These two main chapters of Data reduction are presented in this chapter.

2.3.2 Basic CCD Data reduction

The process of standard CCD image reduction makes use of a basic set of images that forms the core of the calibration and the reduction process. This basic set of images consists of three calibration frames: bias, dark and flat field and the initial data frames of the object of interest.

The use of this basic set of calibration images in the reduction of the object CCD data frames is as follows. First subtract a mean bias frame from the object frame. Then, divide the resulting image by a (bias subtracted) mean flat field image. These two simple processes can correct the basic frame for bias level, dark current and nonuniformity within each image pixel. During the analysis of the object frame, it is likely that background or sky contribution to the image will need to be removed. This correction for the background sky is performed as part of each specific analysis step using sky regions in the object frame itself and it is not removed with some sort of separate sky frame. The calibration process can be written as

$$Final\ Reduced\ Object\ Frame = \frac{Raw\ Object\ Frame - Bias\ Frame}{Flat\ Field\ Frame}$$

Where we should mention again the flat field image has been bias subtracted and the bias frame can be replaced by a dark frame when appropriate.

Bias Image Description: This type of CCD image has an exposure time of zero seconds. The shutter remains closed and the CCD is simply readout. The purpose of a bias or else zero frame is to allow us determine the underlying noise level within each data frame. The bias value in a CCD image is usually a low spatial frequency variation throughout the array, caused by the CCD on-chip amplifiers. This variation should remain constant with time. The rms value of that bias level is the CCD read noise. A bias frame contains both the DC offset level (overscan) and the variations of that level. A single bias frame will not sample these variations well in a statistical fashion, so an average of at least 10 bias images is recommended.

Figure 2.8 A bias frame taken by the reported system.

Dark Image Description: CCD dark frames are images taken with the shutter closed, but with exposure time equal to that of the object frames. Long dark frames can often be avoided using the assumption that the dark current increase linearly with time and the application of a simple scaling. Dark frames are a method by which the thermal noise (dark current) in a CCD can be measured. They also can reveal information about bad or "hot" pixels that exist as well as provide an estimate of the rate of cosmic rays that strike the observing site. Thermoelectrically cooled systems are not cooled to low enough temperatures such as one may ignore the dark current. Multiple dark frames averaged together are the best way to produce the final dark calibration frame. Note that if dark frames are used, the bias level of the CCD is present in them as well, and therefore separate bias frames are not needed.

Figure 2.9 A dark frame taken by the reported system

Flat Field Image Description: Flat field exposures are used to correct for pixel-to-pixel variations in the CCD response as well as any nonuniform illumination of the detector itself. Flat fields expose the CCD to light from either a dome screen, the twilight sky or a projector lamp in an attempt to provide a high Signal to Noise ratio, uniform calibration image. Especially for narrow band imaging, flats are very helpful in removing fringing which may occur in object frames. Flat field calibration frames are needed for each color, wavelength region, or different instrumental setup used in which object frames are to be taken. As with the other calibration frames, more than 5 flat frame fields should be taken and averaged to produced the final flat used for image calibration.

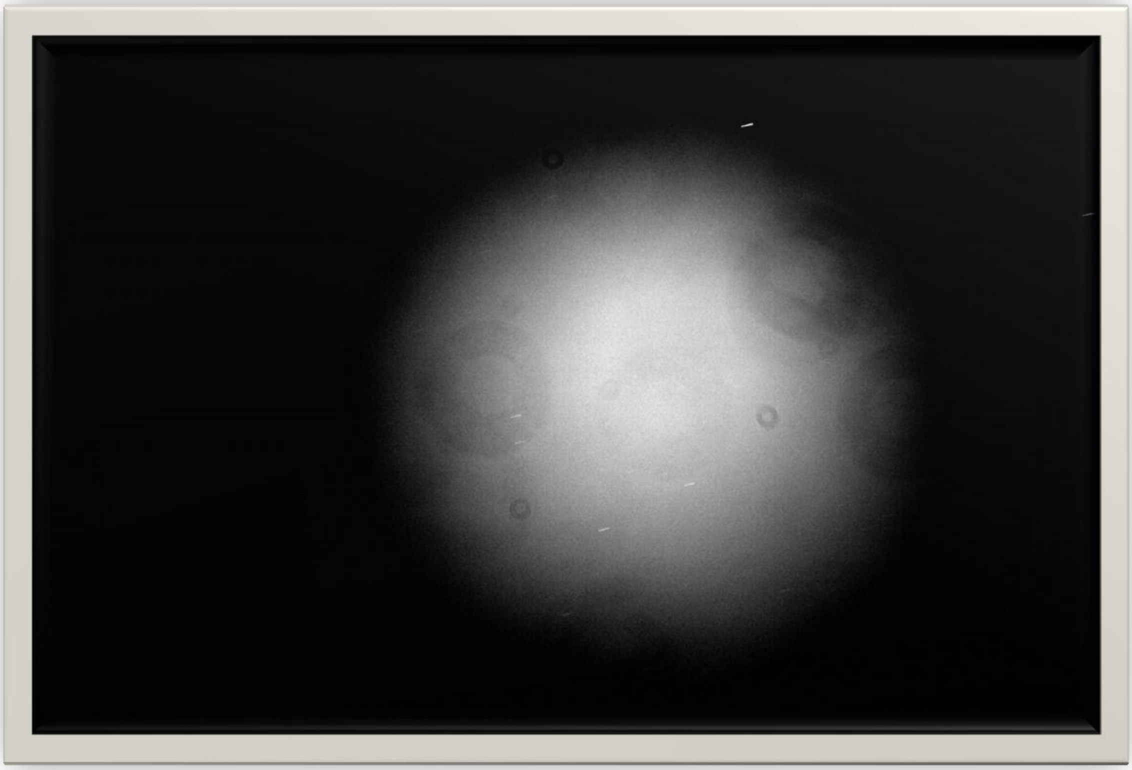

Figure 2.10 A sky flat frame taken by the reported system

Object Frame Image Description: These are the frames containing the astronomical object of interest. Their exposure time range from 1 second or less, up to many hours, varying for reasons of type of science, brightness of object, desired temporal sampling etc. Within each object image pixel are contributions from the object and/or sky, readout noise, thermally generated electrons, and possibly contributions from cosmic rays. Each pixel responds similarly but not exactly equally to the incident light, so nonuniformities must be removed. The majority of noise and spatial factors are correctable to very low levels via standard CCD reduction as described above.

2.3.3 Pixel Binning

The pixel summing process is called binning. Binning has to do with the way the readout of the CCD in which each pixel is read, digitized, and stored. Pixels can be binned (summed) in both vertical and horizontal axis. Binning of 2×2 would mean that an area of 4 adjacent pixels will be binned or summed on chip within the output register during readout. The result of this binning operation will produce one "superpixel" value, which digitized and stored in the final image. The original values of the individual summed pixels are lost forever. If we could add up the charge say 4 pixels before they are digitized , we would get a final signal level equal to ~ 4 times each single pixel's value but only one times the read noise. This process is called on-chip binning.

2.3.4 Data Reduction Software

The software used for Data reduction was GAIA included in the Starlink Package and IRIS image processing software.

GAIA software was used mostly for the recognition of the object frames and also to prepare the frames for perfect alignment through the stacking process. This was succeeded with the use of astrometry on the fields.

The IRIS software was used for all the imaging processes included basic Data reduction, stacking of the frames and continuum subtraction in the manner we later describe.

2.3.5 Continuum Subtraction

In a frame of an astronomical object recorded through a narrow band filter, background continuum light completes the aggregation of photons that are recorded by the CCD chip. Continuum subtraction process aims in isolating the narrow band light from the continuum background.

In order to subtract this light the object frames should also be photographed with a related broad band filter. In our case the filter that is related to the continuum subtraction of OIII line observations, is the Stromgren -y broadband filter that has a FWHM of 23 nm between 535 nm and 560 nm. At this point a matter that has to be considered is the percentage of each subtraction in order to avoid oversubtraction of the main image and loose some valuable photons. We used the equations developed by Roberto Terlevic ("High-resolution surface photometry of the core of NGC 4151, 1991") in order to correct this effect. This has been done by considering the line and continuum contributions to each of the OIII and Stromgren -y filters to the total intensities $I_{(OIII)}$ and $I_{(Sty)}$. To use these equations we have to normalize the frames to ADU's/sec and then estimate the scale factor of the continuum. These equations are shown below:

$$I_{(OIII)} = I_1\, \tau_{(OIII)} + I_C \int_{\Delta OIII} \tau_{(OIII)}(\lambda) d\lambda = I_1\, \tau_{(OIII)} + I_C\, K_{(OIII)}$$

$$I_{(STy)} = I_1\, \tau_{(STy)} + I_C \int_{\Delta STy} \tau_{(STy)}(\lambda) d\lambda = I_1\, \tau_{(STy)} + I_C\, K_{(STy)}$$

Where $I_{(OIII)}$ and $I_{(Sty)}$ are the observed intensities (in Counts/sec) of OIII and of Stromgren -y filters respectively. ΔOIII and ΔSTy are the OIII and Stromgren y filters bandwidth (FWHM in table 3.3) and τ_{OII} and τ_{STy} thecorresponding filter transmissions at the redshifted OIII wavelength (Argyle et al, 1988). The 1 and c indexes denote the OIII emission line and continuum, respectively.

$$K_{(OIII)} = \int_{\Delta OIII} \tau_{(OIII)}(\lambda) d\lambda$$

$$K_{(STy)} = \int_{\Delta STy} \tau_{(STy)}(\lambda) d\lambda$$

Assuming the intensity of the continuum to be constant through the bandwidth and the filter transmission also constant through the line, the intensity of the OIII emission line can be obtained directly as:

$$I_1 = \frac{I_{(OIII)}\,K_{STy} - I_{(STy)}\,K_{OIII}}{\tau_{(OIII)}\,K_{STy} - \tau_{(STy)}\,K_{OIII}}$$

The two frames were aligned using the IRIS program and the "stellar registration" command included in the "processing" general list of commands.

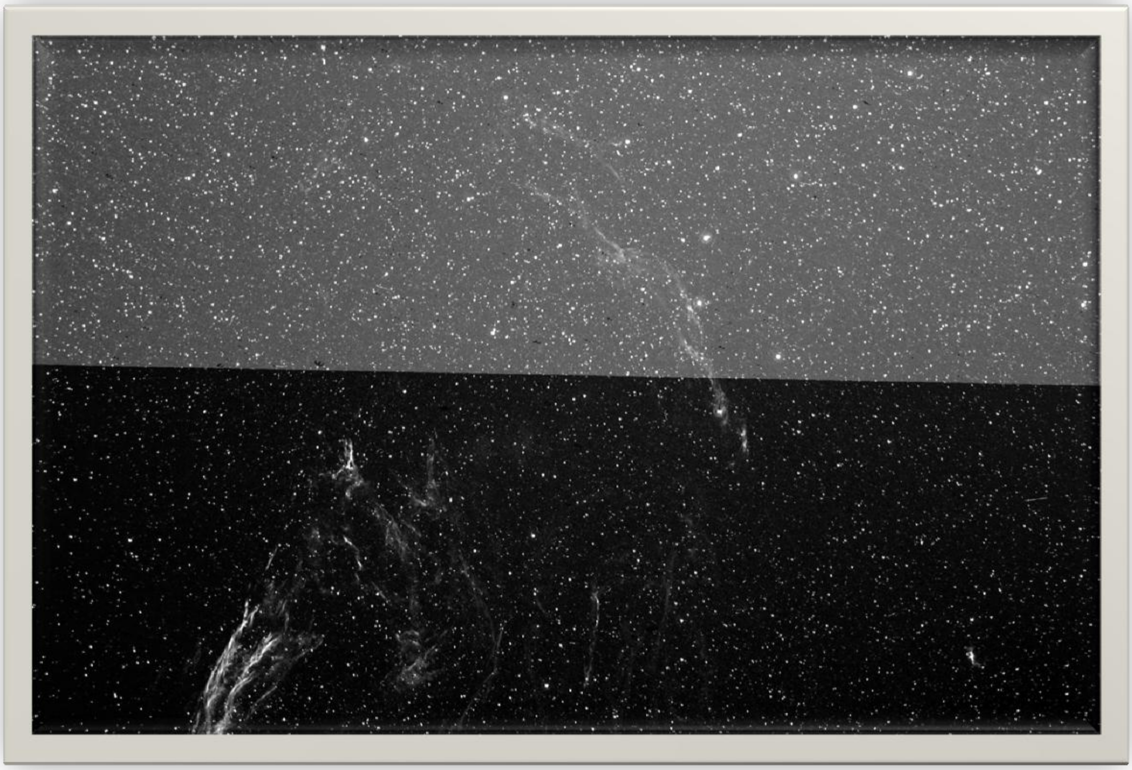

Figure 2.11 This is an example that shows the importance of continuum subtraction in narrow band observations. For this image of Cygnus loop photographed by the author with the OIII narrow band filter. Continuum subtraction used only for the lower part of the image. It is clear that the nebulae filaments are much sharper and in higher contrast with the respect to background.

Chapter 3: Results

In this chapter we are presenting the results of this diploma thesis. The three main targets that we sooner discussed were observed and gave the following results. The success of this diploma thesis relied on the systems configuration wide field. The SNR G74.0-8.5–Cygnus Loop is seen complete for the first time without the need of a mosaic and the image of SNR G82.2+5.3 reveals extended parts of it that were not known in previous studies.

G74.0-8.5 –Cygnus Loop

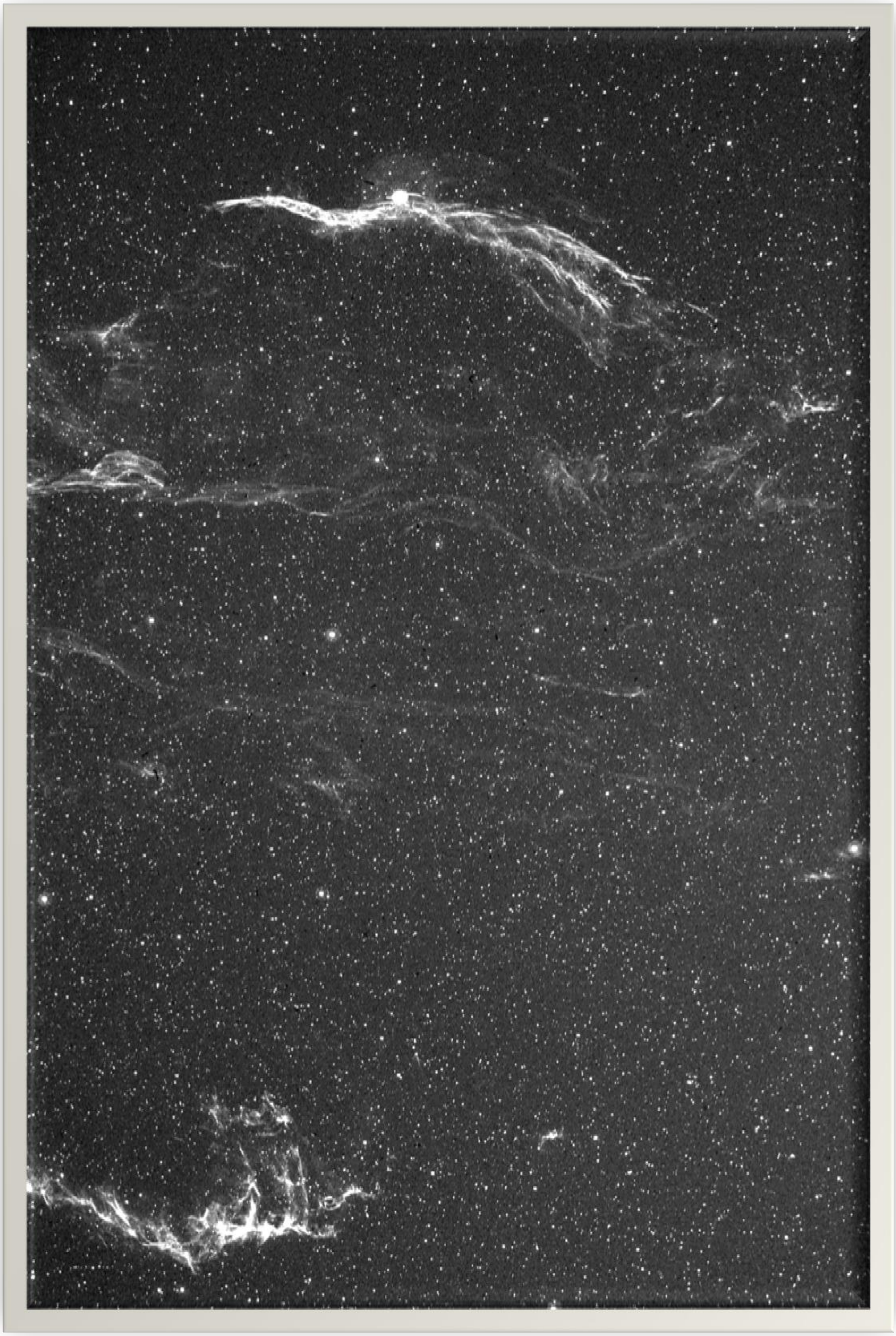

This is an image of SNR G74.0-8.5 centered in RA= $20^h 13^m 00^s$ and Dec= $+36^{\circ} 12'$ with a field of view $3.6835^{\circ} \times 2.1942°$. It is a stack of 3 exposures of 1200 sec giving a combined total of one hour exposure through the $[O_{III}]$ narrow band filter. Also one exposure of 1200 sec through the S*tromgren -y* filter was used in order to achieve the proper continuum subtraction.

The Cygnus loop is a well known, very bright shell type SNR. It is located in the Cygnus constellation and is about 1860 light years away. In this figure we can clearly see almost the complete remnant in one frame, thought it has near 3 degrees of apparent diameter, given the system's wide field ability. The remnant's filamentary structure is also clearly shown.

G82.2+5.3

This is an image of SNR G82.2+5.3 centered in RA= $20^h19^m00^s$ and Dec= $+45^{\circ}30'$ with a field of view $3.6835^{\circ} \times 2.1942°$ degrees. It is a stack of 3 exposures of 1200 sec giving a combined total of one hour exposure through the $[O_{III}]$ narrow band filter. Also one exposure of 1200 sec through the *Stromgren -y* filter was used in order to achieve the proper continuum subtraction.

In this figure we see a much fainter SNR than Cygnus Loop. G82.2+5.3 is a remnant that it is much harder to record due to its inferior brightness and the existence of a nebulae in the same direction that has to be subtracted (figure 1.6). The $[O_{III}]$ image reveals filamentary emission in the west and east areas of the image as well diffuse emission. The two basic filamentary structures define the opposite sides of an ellipsoidal shell.

G93.7-0.2

This is an image of SNR G93.7-0.2 centered in REA= $21^h29^m20^s$ and Dec= $+50^{\circ}50'$ declination with a field of view $3.6835^{\circ} \times 2.1942°$ degrees. It is a stack of 3 exposures of 600 sec giving a combined total of half hour exposure through the $[O_{III}]$ narrow band filter. Also one exposure of 600 sec through the S*tromgren -y* filter was used in order to achieve the proper continuum subtraction.

In this case no SNR is detected. We can only conclude that we need additional observations to detect thus SNR. Please note small trails created by unwanted movement of the telescope during the exposure which made the situation worst.

Bibliography

Βιβλία στα ελληνικά

1- *Χ. Βάρβογλης, Ι.Χ. Σειραδάκης,* Εισαγωγή στην σύγχρονη αστρονομία, Εκδόσεις Γαρταγάνη.
2- *Σ. Αυγολούπης, Ι.Χ. Σειραδάκης*, Παρατηρησιακή αστρονομία, Εκδόσεις Πλανητάριο Θεσσαλονίκης.
3- *H,J,P Arnold,* Αστροφωτογραφία Εκδόσεις Πλανητάριο Θεσσαλονίκης.

Books in English

4-Carroll B. W., Ostlie D. A., An introduction to Modern Astrophysics, Addison Wesley Publishing Company, Inc.

5-Howell B. S., Handbook of CCD Astronomy, Cambridge University Press.

Papers

6-Osterbrock, D.E., Astrophysics of gaseous nebulae and active galactic nuclei, University Science Books, 1989

7-Fesen, R. A.; Blair, W. P.; Kirshner, R. P., Optical emission-line properties of evolved galactic supernova remnants, The Astrophysical Journal, 292: 29-48, 1985

8-Raymond J.C., Shock waves in the interstellar medium, The Astrophysical Journal Supplement Series, 39:1-27, 1979

9-*Luis C. Bohlin R.C.*, Absolute flux calibration of optical spectophotometric standard stars, Astronomical Journal, 1994

10- *Boumis P., Mavromatakis F., and Paleologou E. V..*, First optical light from the supernova remnant G 17.4−2.3, A&A 385, 1042{1048 (2002)

11- *Boumis P., Mavromatakis F., Xilouris E. M., Alikakos,M J.. Redman P., and Goudis C. D.* Deep optical observations of the supernova remnants G 126.2+1.6, G 59.8+1.2 and G 54.4−0.3, A&A 443, 175–183 (2005)

12- Mavromatakis F., Boumis P., Papamastorakis J., and Ventura J. Deep optical observations of G 65.3+5.7, A&A 388, 355{362 (2002)

13- *Mavromatakis F., Boumis P., Papamastorakis J., and Ventura J.* Optical supernova remnant observations from Skinakas Observatory, Science Direct, 2003

14- *Boumis P., Alikakos J., Christopoulou P. E., Mavromatakis F., Xilouris E. M., Goudis C. D.* First optical detection of the supernova remnant G 15.1−1.6, A&A 481, 705–712 (2008)

15- *S. O. Tagieva*, Observational effects in Supernova Remnants associated with H II regions and dense gaseous clouds, Astronomy Letters, Vol. 28, No. 5, 2002, pp. 310–315.

16-*R.J. Salt*, An analysis on visibility based continuum subtraction, A&A Supplement Series, 107:55-69 (1994)

17- *Pavuti, Duric, et al,l* An *X*-Ray, optical and radio search for Supernovae Remnants in the nearby Sculptor group Sd galaxy NGC 300, THE ASTROPHYSICAL JOURNAL, 544:780È804, 2000

18- Terlevich, R et all, High-resolution surface photometry of the core of NGC 4151, Royal Astronomical Society, Monthly Notices (ISSN 0035-8711), vol. 249, March 1, 1991, p. 36-45

Websites

http://imagine.gsfc.nasa.gov/docs/science/know_l2/supernova_remnants.html

http://www.phy.duke.edu/~kolena/snrspectra.html